Extraction of fragments and waves after impact damage in particle-based simulations

Patrick Diehl and Michael Bußler and Dirk Pflüger and Steffen Frey and Thomas Ertl and Filip Sadlo and Marc Alexander Schweitzer

1 Introduction

Peridynamics is a generalization of traditional continuum mechanics. It is a particle-based approach and targeted towards the modeling of fractures and similar phenomena. The fundamental equations are integral equations. Damage is modeled by a force function that acts between two particles each.

Using peridynamic simulations, a vast range of materials with different properties, from polymethyl methacrylate to titanium alloy can be simulated [5]. The results significantly depend on the models and numerical schemes that are employed. Different models for bonds, time integration schemes and the summation of forces between particles are employed. Furthermore, several parameters such as the interaction horizon of particles can be tuned.

Patrick Diehl and Marc Alexander Schweitzer
Institute for Numerical Simulation, Wegelerstraße 6, 53115, Bonn, Germany, e-mail: (diehl,schweitzer)@ins.uni-bonn.de

Michael Bußler,Steffen Frey, and Thomas Ertl
University of Stuttgart Visualisation Research Centre, Allmandring 19, 70569, Stuttgart, Germany e-mail: (Michael.Bussler,Steffen.Frey,Thomas.Ertl)@visus.uni-stuttgart.de

Dirk Pflüger
IPVS/SGS, Universitätsstraße 38, 70569, Stuttgart, Germany e-mail: Dirk.Pflueger@ipvs.uni-stuttgart.de

Filip Sadlo
Interdisciplinary Center for Scientific Computing, Im Neuenheimer Feld 368, 69120, Heidelberg, Germany e-mail: filip.sadlo@iwr.uni-heidelberg.de

Marc Alexander Schweitzer
Meshfree Multiscale Methods, Fraunhofer SCAI, Schloss Birlinghoven, Konrad-Adenauer-Straße, 53757 Sankt Augustin, Germany

To study a certain material, the simulation results have to be validated and verified [3]. However, this is not a trivial task in itself. A common experimental benchmark is the Kalthoff-Winkler experiment [7], which was studied in [18, 22]. First, and where available or possible, simulation results can be verified against experiments [4, 1, 2]. Second, and much more frequent in the literature, metrics obtained in the simulation are compared against analytic results [11] – once again, only where possible – or against simulation results using different modeling approaches. It is obvious that characteristic numbers that can be measured by experiments cannot necessarily be obtained by analytic equations and vice versa.

Simulations, in contrast, have the advantage that metrics for both worlds can be obtained. Of course, this poses extra challenges. It is easy to obtain the size of fragments in scattering scenarios; characterizing their shapes requires significantly more effort. And the extraction of continuous measures such as the speed of stress propagation in a discrete and three-dimensional simulation world requires good interpolation techniques and careful analysis.

To provide a first, fast validation to simulation results, instructive visual feedback is more than helpful. A typical approach to quickly examine the effect of changes in the model or its parameters is to plot the particles and to color them depending on the local damage, for example. While this gives a quick impression on the damage behavior, it is restricted to the surface. It neither shows where a crack penetrates through the whole material, nor provides insight into what happens within the material. This basic visualization approach is already sufficient to study crack branching or the velocity at the crack tip, as demonstrated in the experiments in [21, 9]. For complex structures and other metrics, more advanced techniques are required.

In this work, we have developed and adapted methods to analyze impact damage in particle-based simulations [10, 12, 15]. Furthermore, we show their illustrative visualization and demonstrate its instructive power. This is a major step towards the future verification and validation of our models. We have focused on the analysis of fragmentation via fragment analysis and on impact damage via the propagation of stress waves.

1.1 Fragmentation

An important validation for particle-based methods is the identification of fragments after impacts, like a stone impacting the front window of a car. Here the size of the fragments is an important metric to estimate the medical harm to the occupants. Obtaining the relevant quantities, such as the size, mass and velocity of each fragment is still difficult in experiments. The experiment [26] provides a distribution for the number of fragments with respect to the fragment mass. The setup is a tungsten-alloy projectile perforating a steel armor plate with a velocity of $1020\,\mathrm{m\,s^{-1}}$. This

experimental data is used as a benchmark for the smoothed particle hydrodynamics (SPH) model in [29] and for a Lagrangian approach in [17]. Another experiment covered in the literature is the fragmentation of a cylindrical steel tube using a gas gun impact with the velocity of $1920\,\mathrm{m\,s^{-1}}$ [28]. This experimental data is used as a benchmark for SPH [13]. All of these benchmarks show that fragmentation obtained by the simulations are qualitatively reasonable, but that the quantitative modeling of the material needs some improvement.

1.2 Impact damage and wave propagation

For the safety of crashes with electric/hybrid cars, the impact damage in the ceramic core of the battery is essential. A common benchmark for the impact damage and wave propagation in ceramic material is the edge-on impact (EOI) experiment [20, 27, 8], which was developed in the 1980s for the visualization of impact damage and wave propagation. Different particle-based material models were verified against this experiment [19, 2]. Here, the reflection and interference of the impact shock wave is of high importance to understand where the damage in the ceramic core occurs.

In the remainder, we will first describe peridynamics in Section 2 and our visualization approaches in Section 3. In Section 4 we introduce experiments and explain their (visual) analysis. Finally, Section 5 concludes the work.

2 Peridynamics

As a reference particle-based method we consider peridynamics (PD), which is a non-local generalization of continuum mechanics, with a focus on discontinuous solutions as they arise in fracture mechanics. In this section, we present the essential ingredients that are important for the visualization techniques. The principle of this theory is that particles interact with other particles at a finite horizon δ by exchanging forces. This is very similar to SPH and MD approaches. The bond-based peridynamics equation of motion [23] for the acceleration at time t is given by the integral equation

$$\varrho(X)A(t,X) = \int\limits_{B_\delta(X)} f(t, x(t,X') - x(t,X), X' - X)dX' + b(t,X), \qquad (1)$$

with the mass density $\varrho(X)$, f as the pair-wise force function which models the interaction of particles X and X' with respect to the initial reference configuration Ω_0, and with $b(t,X)$ denoting the external force. The internal forces between particles are exchanged within the finite interaction zone $B_\delta(X)$, see Figure 1. As the constitutive law we use the Prototype Brittle Microelastic (PMB) material law [24] and for the simulations we use LAMMPS [16]. The bond-based PD, where a bond between two

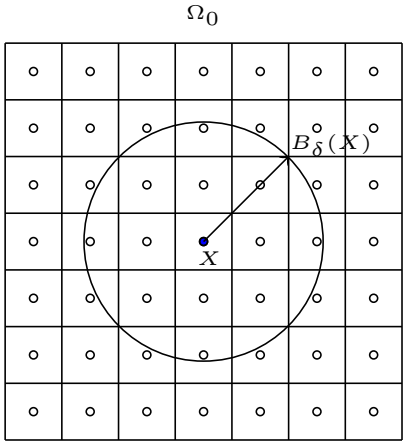

Fig. 1: The reference configuration Ω_0 at time $t = 0$ with the finite interaction zone of length δ for particle at position X. All particle inside the interaction zone $B_\delta(X)$ of particle X are connected with bonds to exchange forces.

particles X and X' responds independently of all other bonds inside the interaction zone $B_\delta(X)$, implies that the Poisson ratio of the isotropic linear elastic solid is restricted to $\nu = 1/4$ for 3D and $1/3$ for 2D. Within the state-based PD, all other bonds connected to the endpoints of particle X influence the stretch and thus, any material, which is described by the classical continuum mechanic, can be modeled [25]. For the state-based PD, the equation of motion (1) is replaced by the following integral equation

$$\varrho(X)A(t,X) = \int_{B_\delta} \{\mathbf{T}[t,X]\langle X' - X\rangle - \mathbf{T}[t,X']\langle X - X'\rangle\}\, dX' + b(t,X) \qquad (2)$$

where $\mathbf{T}$ is the force vector state field. Cracks and fractures are modeled by the breaking of bonds between particles. Here a critical stretch s_c for bond breaking is predefined for all particles, and the bond between two particle breaks irreversibly if the stretch surpasses the predefined critical value. The ratio of the existing bonds inside the interaction zone $B_\delta(X)$ and the amount of bonds inside $B_\delta(x)$ at the reference configuration Ω_0 describes the damage $c(t,X)$ of a particle. For the simulation we used an extended version of Peridigm [14] and the elastic material model.

Table 1 shows for each particle at position X in the reference configuration Ω_0 the attributes available at each time step for the post-processing in the visualization pipeline. We extended Peridigm with a compute class for the adjacency matrix M_t, so that all bonds between particles are available as an additional information for the post-processing pipeline. Fore more details about peridynamics and material models we refer to [25, 23, 24].

Attribute	Symbol	Unit
Acceleration	$a(t, X) \in \mathbb{R}^3$	ms^{-2}
Actual position	$x(t, X) \in \mathbb{R}$	m
Density	$\varrho(X) \in \mathbb{R}$	$\mathrm{kg\,m}^{-3}$
Damage	$c(t, X) \in \mathbb{R}$	‰
Displacement	$D(t, X) := \lvert X - x(t, X)\rvert \in \mathbb{R}^3$	m
Initial position	$X \in \mathbb{R}^3$	m
Force	$f(t, X) \in \mathbb{R}^3$	N
Velocity	$v(t, X) \in \mathbb{R}^3$	ms^{-1}
Volume	$V(X) \in \mathbb{R}$	m^3
Stress	$\sigma(t, X) \in \mathbb{R}^6$	Pa

Table 1: Attributes per particle X, which where used in the post-processing pipeline for the extraction of the fragments and fracture surface.

3 Visualization techniques

We present two visualization techniques for the analysis of data resulting from peridynamics simulations. The first technique discusses how the data describing fractures can be separated into fragments, revealing the shape and size of the fragments. The second technique describes the visualization of the stress tensor and is used to visualize the wave propagation after impact damage.

3.1 Clustering

For the visualization, it is important to identify each individual fragment. We therefore apply a connected components labeling (Algorithm 1). It iterates over all particles in a given time step t and identifies fragments by specifying a label for each particle, so that particles that belong to the same fragment share a common label. We use two criteria in the algorithm to identify connectivity between particles, the maximum damage value s and the maximum bond length r. Thus, the initial displacement between two particles X and X' is not larger than $\|X' - X\| \leq r$ for connected components. Note, that the maximum bond length and critical damage s are parameters to influence the fragmentation of the algorithm and the horizon δ and the critical stretch s_c are independent model parameters.

Algorithm 1: Component Labeling

Input: particles P, bonds B, max damage value s, max bond length r, time t
Output: every particle labeled by piece id of connected component

```
1  for every particle n do
2      label[n] ← 0 ;
3      visited[n] ← false ;
4  n ← 0 ;
5  while n < |P| and c(t, X_n) > s do
6      visited[n] ← true;
7      n ← n + 1;
8  currentLabel = 1;
9  Stack S;
10 while n < |P| do
11     label[n] ← currentLabel ;
12     visited[n] ← true;
13     S ← n ;
14     while S ≠ ∅ do
15         n' ← S;
16         C ← getConnectedParticles(n', B);
17         for n'' ∈ C do
18             if not visited[n''] and distance(n',n'') < r and c(t, X_n'') < s then
19                 label[n''] ← currentLabel;
20                 visited[n''] ← true;
21                 S ← n'';
22     while n < |P| and (visited[n] or c(t, X_n) > s) do
23         visited[n] ← true;
24         n ← n + 1;
25     currentLabel ← currentLabel + 1;
```

By specifying the maximum bond length, we can restrict the search of connected components to those particles that are in direct neighborhood to each other. The maximum damage value s is required, as the given set of bonds contains both active and broken bonds. Therefore, we could not rely for our analysis of connected components solely on the connections of particles through bonds, as this would require a set of bonds containing only the active part. Still, we found that filtering out particles by a user-specified maximum damage value gives good results for the identification of fragments. For our experiments, we used a maximum damage value of $s = 0.2$ and a maximum bond length of $r = 0.001$.

All particle labels are initialized with id 0 (Line 2). This id is also used to identify particles that do not belong to a fragment, as their label id is not altered by the algorithm. We also store a flag for each particle (Line 3), which specifies whether the particle was already visited to avoid infinite loops while traversing through the connections. In lines 4–7, the algorithm iterates over all particles to find the first

particle whose damage value is below the given threshold s. This particle belongs to the first fragment and is labeled with the current label id (Line 11). Next, the particle is pushed on a stack (line 13), which is used to traverse all particles connected to the given particle. The traversal, Lines 14–21, is done by testing for each connected particle to see whether it has not been visited and meets the criteria for maximum distance r and damage threshold s (Line 18). If so, the particle is labeled with the current label id and also pushed on the stack. This step is repeated until the stack is empty and all connected particles have been visited. In Lines 22–24, the next component is identified by searching for a particle that has not been visited yet and that meets the damage criterion s. These steps are repeated until all particles have been visited and a label specified for each particle.

3.2 Visualization of the stress tensor

To highlight the waves after an impact damage, we visualize the stress tensor $\sigma(t, X)$, defined for each particle position X and time step t, by means of the spectral norm of the stress tensor. The scalar-valued spectral norm of a tensor A is given as the square root of the largest eigenvalue $\lambda_{\max}$ of A^*A,

$$\|A\|_2 = \sqrt{\lambda_{\max}(A^*A)}, \tag{3}$$

where A^* denotes the transpose of A.

The first step in the visualization pipeline is to calculate and store the spectral norm of the stress tensor for each particle. In the next step, the resulting scalar values given at the particle positions are resampled on a Cartesian grid using inverse distance weighting to obtain a continuous distribution of the spectral norm over the whole domain. For the resampling step, we use a grid resolution of $200 \times 200 \times 200$ and a maximum distance of 0.005. The resulting scalar field is visualized using standard volume rendering techniques.

4 Experiments and their visual analysis

4.1 Fragments and histograms

Figure 2 shows the geometry of a thin plate with a material density ϱ of $2200\,\mathrm{kg\,m^{-3}}$, a bulk modulus K of 14.9×10^9 Pa, and a shear modulus G of 8.9×10^9 Pa. The spherical projectile is modeled as steal with a material density ϱ of $7700\,\mathrm{kg\,m^{-3}}$, a bulk modulus K of 160×10^9 Pa, and a shear modulus G of 78.3×10^9 Pa, and it hits the target with a velocity of $200\,\mathrm{m\,s^{-1}}$. For the simulation with Peridigm, we use the elastic material model, the critical stretch damage model with a critical stretch

$s_c = 0.0025$, and for the interaction of the sphere and the plate a contact model with a spring constant of 1×10^{12}.

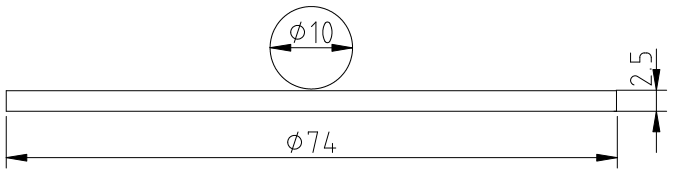

Fig. 2: Blueprint of the thin plate and the spherical projectile.

Figure 3 shows a common visualization of particle-based simulations in the first column. Here, spheres are placed at the center of the actual position $x(t, X)$ of the particles over the time t. These spheres are colorized with the scalar damage value $c(t, X)$ of the particle. Blue indicates that there is no damage, and red indicates that all bonds inside the interaction zone $B_\delta(X)$ are broken. After the impact, the damage develops radially from the center of the plate and starts to bifurcate twice before hitting the boundary of the plate. At the final time step $t = 8.27 \times 10^{-7}$, there are plenty of "free" particles in the center of the plate that have no neighbors inside the interaction zone any more. Additionally, there are some "free" particles between these non-damaged particles. This somehow indicates that the crack resides and that the plate is scattered in different parts. With this particle-based visualization approach we can study how the damage develops through the material and observe different bifurcations of the cracks.

A plain visualization of the particles does not expose information about the shape of fragments or where exactly the crack path develops. Therefore Algorithm 1 is applied on the particle data to cluster the particles to fragments and label them. In the second column of Figure 3, fragments that have been extracted this way are colored by their label. This exposes the shape of the fragments and visualizes the crack pattern in a clear way, see Figure 3(d).

Furthermore, auxiliary attributes like the mass or the velocity at the center of mass of the fragments are of interest. Figure 4 shows the histograms of the fragments' sizes delivered by the algorithm. Here, the algorithm needs to be extended to estimate the mass of the fragment via the density ϱ of the particles and their volumes V. With this additional information, the histograms could be compared to the examples [26, 28] described in Subsection 1.1. Furthermore, a study of the sensitivity of the initial positions X of the particles with respect to the fragment size is important, because the crack pattern looks slightly different for different initial placements of the particles X [6]. Here, the histograms could be used to verify if the distribution of the size is sensitive to the initial position of the particles.

To compare with experiments, the algorithm needs to be improved. For example, the computational effort for the extraction of the fragments needs to be reduced.

The geometry of the projectile and the specimen are more complex than in our experiment here and the amount of particles increases. Due to the slow convergence of particle-based methods, the run-time is then not negligible any more.

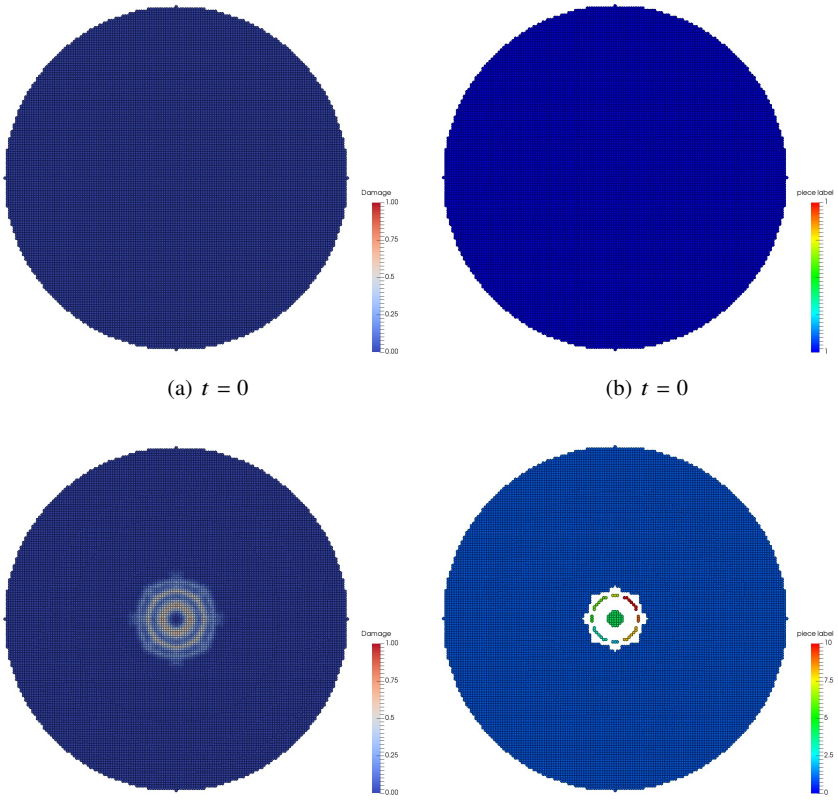

(a) $t = 0$ (b) $t = 0$

(c) $t = 1.27 \times 10^{-7}$ (d) $t = 1.27 \times 10^{-7}$

Fig. 3: Impact of a spherical projectile on a thin plate with a velocity of $200\,\mathrm{m\,s^{-1}}$. The nine figures at the left-hand side (above and below) show the visualization of the particles as spheres colorized with their damage $c(t, X)$. The right-hand side shows the particles colorized according to the extracted fragments.

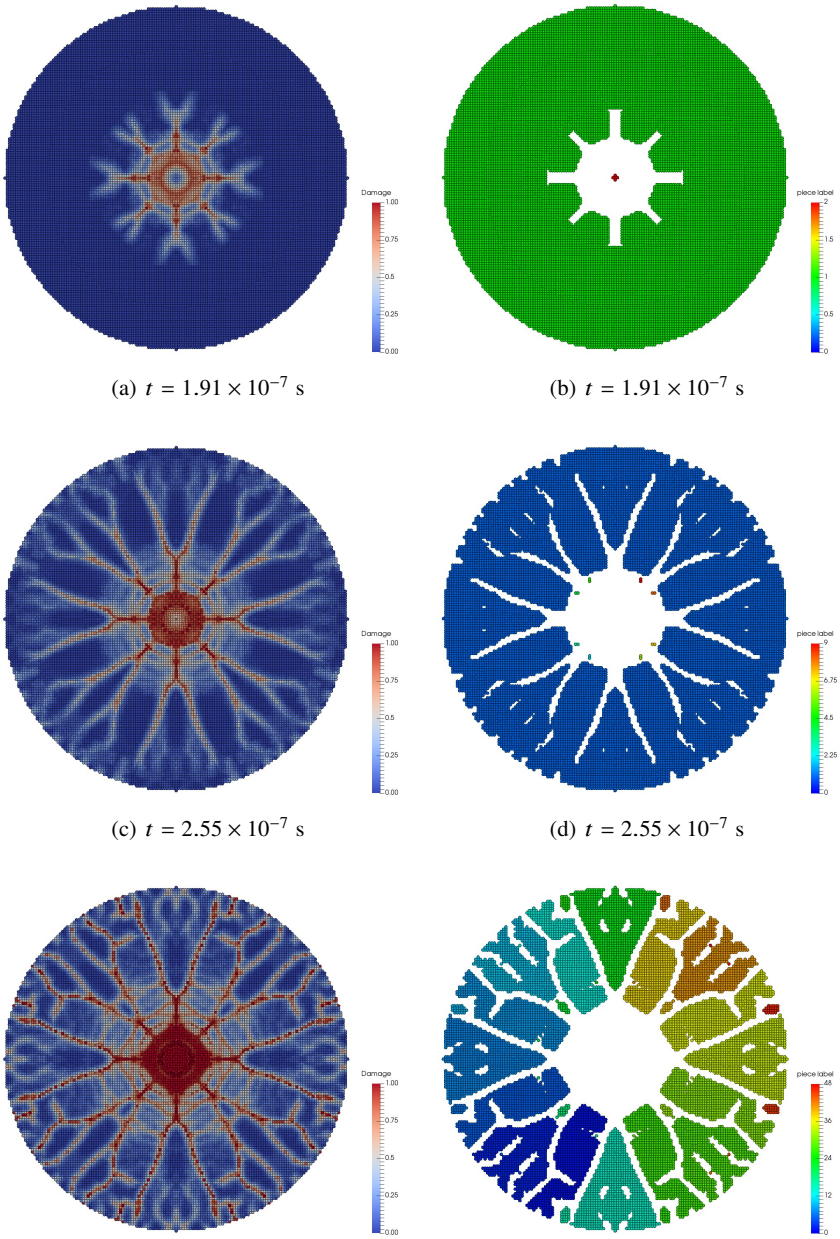

(a) $t = 1.91 \times 10^{-7}$ s (b) $t = 1.91 \times 10^{-7}$ s

(c) $t = 2.55 \times 10^{-7}$ s (d) $t = 2.55 \times 10^{-7}$ s

(e) $t = 3.18 \times 10^{-7}$ s (f) $t = 3.18 \times 10^{-7}$ s

Fig. 3: Impact of a spherical projectile on a thin plate with a velocity of 200 m s^{-1}. The nine figures at the left-hand side (above and below) show the visualization of the particles as spheres colorized with their damage $c(t, X)$. The right-hand side shows the particles colorized according to the extracted fragments.

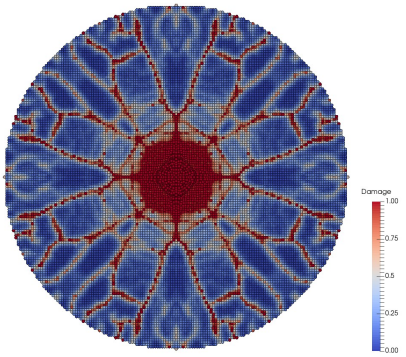

(g) $t = 3.82 \times 10^{-7}$ s

(h) $t = 3.82 \times 10^{-7}$ s

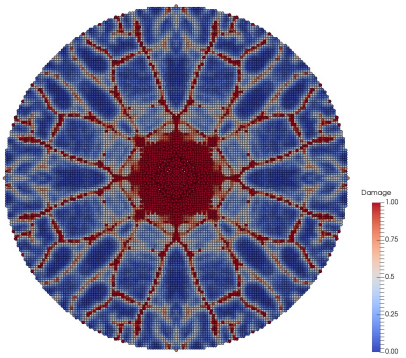

(i) $t = 4.45 \times 10^{-7}$ s

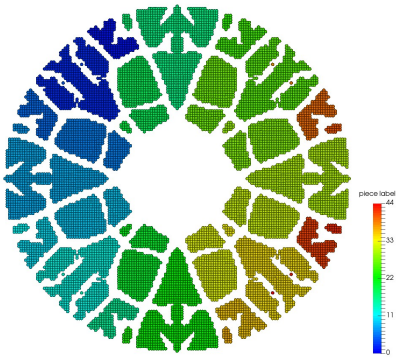

(j) $t = 4.45 \times 10^{-7}$ s

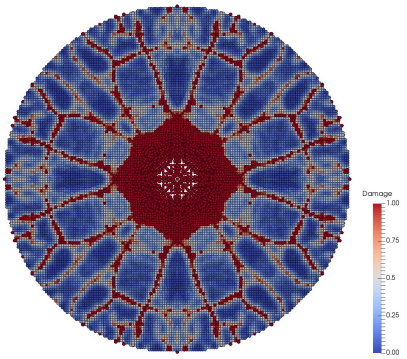

(k) $t = 8.27 \times 10^{-7}$ s

(l) $t = 8.27 \times 10^{-7}$ s

Fig. 3: Impact of a spherical projectile on a thin plate with a velocity of 200 m s^{-1}. The nine figures at the left-hand side (above and below) show the visualization of the particles as spheres colorized with their damage $c(t, X)$. The right-hand side shows the particles colorized according to the extracted fragments.

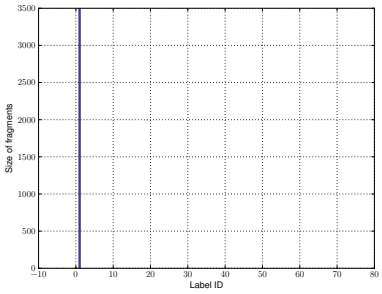

(m) $t = 6.36 \times 10^{-8}$ s

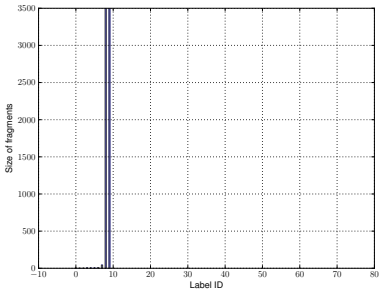

(n) $t = 1.27 \times 10^{-7}$ s

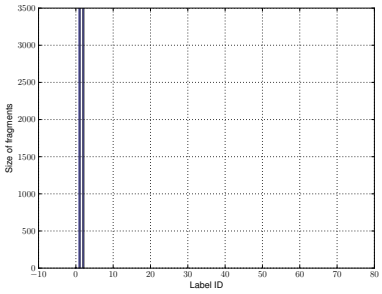

(o) $t = 1.91 \times 10^{-7}$ s

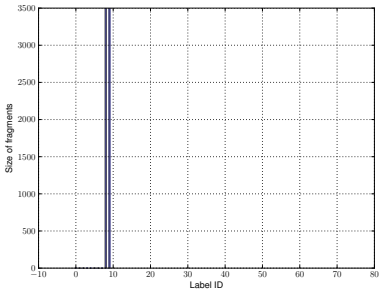

(p) $t = 2.55 \times 10^{-7}$ s

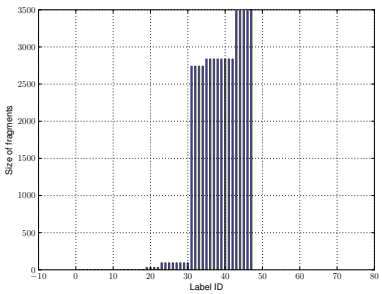

(q) $t = 3.18 \times 10^{-7}$ s

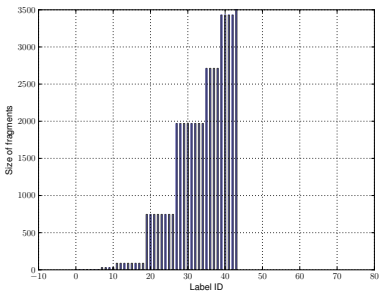

(r) $t = 3.82 \times 10^{-7}$ s

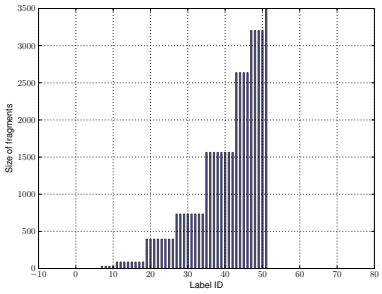

(s) $t = 4.45 \times 10^{-7}$ s

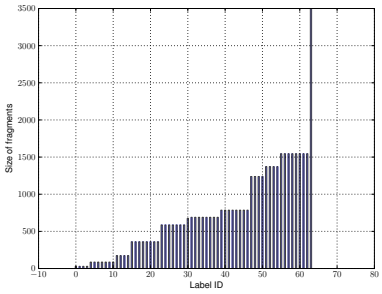

(t) $t = 8.27 \times 10^{-7}$ s

Fig. 4: Distribution of the fragments with respect to the amount of particles per fragment.

4.2 Impact damage and wave propagation

The understanding of wave propagation after impact damage is important to see how the damage front propagates through the specimen and reflects at the boundary. The interference pattern after the reflection of the wave at the boundary is of great interest. Figure 5(a) shows the reconstructed surfaces of the Stanford bunny, a data set of the Stanford 3D scanning repository[1], scanned from a ceramic figurine of a rabbit. For

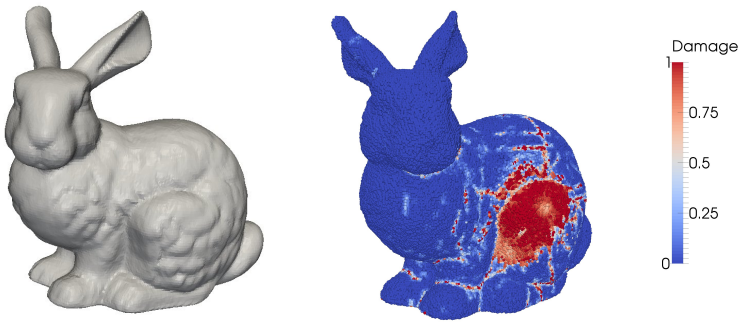

(a) The reconstructed surfaces of the Stanford bunny.

(b) Visualization of the impact damage per particle of the Stanford bunny.

Fig. 5: Figure (a) shows the extracted surfaces of the Stanford bunny as a complex geometry for the simulation and analysis, and Figure (b) shows the impact damage where the spheres at the actual positions $x(t, X)$ are colorized by the damage $c(t, X)$.

this complex geometry, the visualization of the particles and the scalar damage value $c(t, X)$ is not sufficient to see the propagation of the wave through the material (See, Figure 5(b)). For the simulation in LAMMPS, we scattered the surface data set of the bunny with 1 787 245 particles and defined the material with a material density ϱ of $3369\,\mathrm{kg\,m^{-3}}$, a bulk modulus K of 210×10^9 Pa and a critical stress intensity factor K_{Ic} of $2 \times 10^6\,\mathrm{Pa}\sqrt{\mathrm{m}}$.

Figure 6 shows the development of the wave after the impact through the bunny visualized with the technique described in Subsection 3.2. The visualization of the spectral norm of the stress $\sigma(t, X)$ provides a more global view of the propagation, reflection and interference of the wave after the impact damage. Figure 6(f) shows the development of the wave after the impact of the projectile. The arrival of the wave at the back of the bunny is visible in Figure 6(h) (colored in red). The interference of the reflected wave is shown in Figure 6(l), and in Figure 6(i) artifacts at the occiput and the lugs of the bunny are clearly evident.

[1] http://graphics.stanford.edu/data/3Dscanrep/

(a) $t = 0$ s (b) $t = 10^{-8}$ s (c) $t = 5 \times 10^{-8}$ s

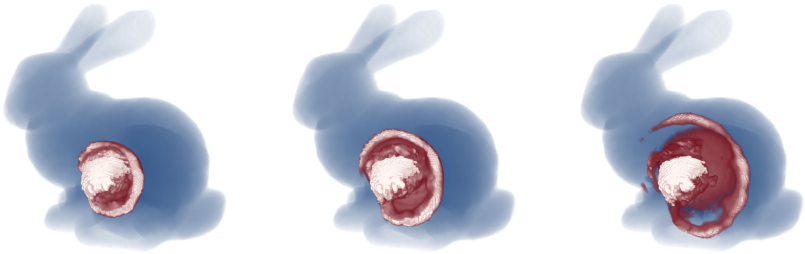

(d) $t = 7 \times 10^{-8}$ s (e) $t = 9 \times 10^{-8}$ s (f) $t = 12 \times 10^{-8}$ s

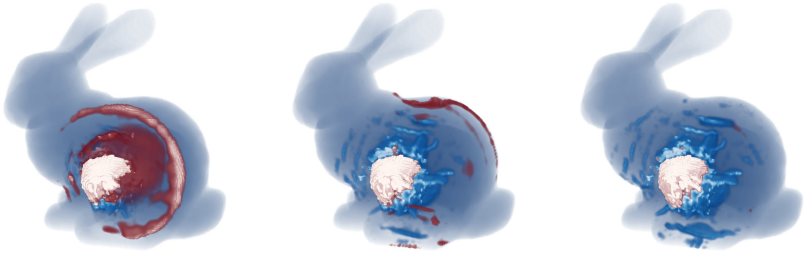

(g) $t = 14 \times 10^{-8}$ s (h) $t = 20 \times 10^{-8}$ s (i) $t = 25 \times 10^{-8}$ s

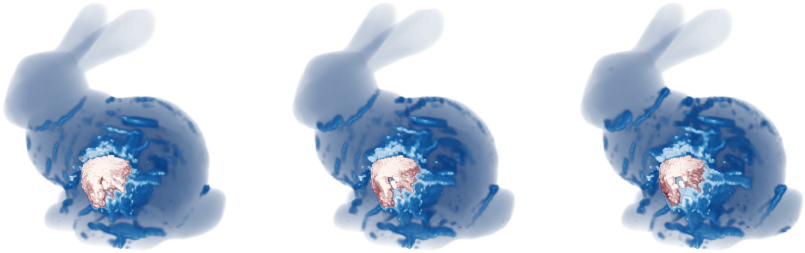

(j) $t = 30 \times 10^{-8}$ s (k) $t = 35 \times 10^{-8}$ s (l) $t = 40 \times 10^{-8}$ s

Fig. 6: Visualization of the stress in the Stanford bunny (1 787 245 particles) with a spherical projectile with an impact velocity of 100 m s^{-1} and a time step size of 10^{-8}.

(a) $t = 45 \times 10^{-8}$ s (b) $t = 50 \times 10^{-8}$ s (c) $t = 55 \times 10^{-8}$ s

(d) $t = 60 \times 10^{-8}$ s (e) $t = 65 \times 10^{-8}$ s (f) $t = 70 \times 10^{-8}$ s

(g) $t = 75 \times 10^{-8}$ s (h) $t = 80 \times 10^{-8}$ s (i) $t = 85 \times 10^{-8}$ s

(j) $t = 90 \times 10^{-8}$ s (k) $t = 95 \times 10^{-8}$ s (l) $t = 100 \times 10^{-8}$ s

Fig. 6: Visualization of the stress in the Stanford bunny (1 787 245 particles) with a spherical projectile with an impact velocity of 100 m s^{-1} and a time step size of 10^{-8}.

5 Conclusion

We presented an approach to extract fragments from particle-based peridynamics simulations. The algorithm delivers fragments as connected components of the particles. Our results show details about the cracks' branches between the fragments, and they provide additional information about the resulting fragments, which are much less obvious in straightforward visualizations. The histograms of the fragment sizes are essential to compare the simulations results to experiments. In the experiments in [26, 28], the mass of the fragments or the velocity at the center of mass of each fragment are provided. To compare the simulations to these experiments, the algorithm needs to be slightly extended to determine the mass of the fragments and the center of mass of a fragment. With these additional attributes, the sensitivity of the initial positions to the distribution of the mass could be addressed. We planing such a comparison as future work.

Capturing the impact damage and wave propagation in brittle materials is done with high-speed cameras [20, 27, 8]. Here, the benchmark with particle-based simulations is a challenge, because the velocity is available per particle. The results of these experiments are the velocity at the wave front or damage front. With our visualization technique , the propagation and inference of the waves after the impact is visualized in the volume of the geometry. Thus, a more "global" view of the waves can be achieved compared to standard visualization. However, the propagation of the waves is not qualitatively comparable with the shadow graphs provided in the experiment with the high-speed cameras. For a quantitative comparison to the experiments, the visualization techniques need to be extended to obtain the velocity at the wave front.

For both approaches, the visualization delivers new intuitive and instructive aspects for analyzing the simulation results qualitatively with new insights in the fragmentation and the propagation of the wave after the impact damage. Both approaches have to be slightly extended for a quantitative comparison of experiments in the future.

References

1. Florin Bobaru and Guanfeng Zhang, *Why do cracks branch? a peridynamic investigation of dynamic brittle fracture*, International Journal of Fracture (2016), 1–40.
2. P. Diehl and M. A. Schweitzer, *Simulation of wave propagation and impact damage in brittle materials using peridynamics*, Recent Trends in Computational Engeneering – CE2014 (Miriam Mehl, Manfred Bischoff, and Michael Schäfer, eds.), Lecture Notes in Computational Science and Engeneering, Springer, 2015.
3. J. Fineberg and M. Marder, *Instability in dynamic fracture*, Physics Reports **313** (1999), no. 1–2, 1 – 108.
4. J.T. Foster, *Dynamic crack initiation toughness: Experiments and peridynamic modeling*, Ph.D. thesis, Purdue University, 2009.
5. Fabian Franzelin, Patrick Diehl, and Dirk Pflüger, *Non-intrusive uncertainty quantification with sparse grids for multivariate peridynamic simulations*, Meshfree Methods for Partial Differential Equations VII (Michael Griebel and Marc Alexander Schweitzer, eds.), Lecture Notes in Computational Science and Engineering, vol. 100, Springer International Publishing, 2015, pp. 115–143 (English).
6. Steven F. Henke and Sachin Shanbhag, *Mesh sensitivity in peridynamic simulations*, Computer Physics Communications **185** (2014), no. 1, 181 – 193.
7. J.F. Kalthoff and S. Winkler, *Failure mode transition at high rates of shear loading*, CHiem CY (H.D. Kunze and L.W. Meyer, eds.), vol. 1, DGM Informationsgesellschaft Verlag, 1988, pp. 185–195.
8. N. Kawai, S. Zama, W. Takemoto, K. Moriguchi, K. Arai, S. Hasegawa, and E. Sato, *Stress wave and damage propagation in transparent materials subjected to hypervelocity impact*, Procedia Engineering **103** (2015), 287 – 293, Proceedings of the 2015 Hypervelocity Impact Symposium (HVIS 2015).
9. Akira Kobayashi, Nobuo Ohtani, and Tadashi Sato, *Phenomenological aspects of viscoelastic crack propagation*, Journal of Applied Polymer Science **18** (1974), no. 6, 1625–1638.
10. J. A. Levine, A. W. Bargteil, C. Corsi, J. Tessendorf, and R. Geist, *A peridynamic perspective on spring-mass fracture*, Proceedings of the ACM SIGGRAPH/Eurographics Symposium on Computer Animation (Aire-la-Ville, Switzerland, Switzerland), SCA '14, Eurographics Association, 2014, pp. 47–55.
11. E. Madenci and E. Oterkus, *Peridynamic Theory and its Applications*, ch. Benchmark Problems, pp. 151–166, Springer, 2013.
12. James F. O'Brien, Adam W. Bargteil, and Jessica K. Hodgins, *Graphical modeling and animation of ductile fracture*, Proceedings of ACM SIGGRAPH 2002, ACM Press, August 2002, pp. 291–294.
13. J. M. Owen, *SPH and Material Failure*, Proceedings from the 5LC 2005, 2005.
14. M. L. Parks, D.J. Littlewood, J. A. Mitchell, and S. A. Silling, *Peridigm Users' Guide*, Tech. Report SAND2012-7800, Sandia National Laboratories, 2012.
15. Mark Pauly, Richard Keiser, Bart Adams, Philip Dutré, Markus Gross, and Leonidas J. Guibas, *Meshless animation of fracturing solids*, ACM Trans. Graph. **24** (2005), no. 3, 957–964.
16. Steve Plimpton, *Fast parallel algorithms for short-range molecular dynamics*, Journal of Computational Physics **117** (1995), no. 1, 1 – 19.
17. Johnson G. R., C.A. Gerlach Stryk R.A., Holmquist T.J., and Rowe N.L., *A quantitative Assesment of computational results for behind armor Debris*, 23^{rd} International Symposium On Ballistics, April 2007.
18. S. Raymond, V. Lemiale, R. Ibrahim, and R. Lau, *A meshfree study of the kalthoff–winkler experiment in 3d at room and low temperatures under dynamic loading using viscoplastic modelling*, Engineering Analysis with Boundary Elements **42** (2014), 20 – 25, Advances on Meshfree and other Mesh reduction methods.
19. W Riedel, S. Hiermaier, and K Thoma, *Transient stress and failure analysis of impact experiments with ceramics*, Materials Science and Enginnering B, vol. 173, ELSEVIER, 2010, pp. 139–147.

20. H. Schradin, *Physikalische Vorgänge bei hohen Belastungen und Belastungsgeschwindigkeiten (Physical Processes at High Loadings and Loading Rates)*, Scripts for German Academy for Aeronautical Research, vol. 40, 1939, pp. 21–68.
21. E. Sharon and J. Fineberg, *Universial features of the microbranching instability in dynamic fracture*, Philosophical Magazine B **78** (1998), no. 2, 243–251.
22. S. A. Silling, *Dynamic fracture modeling with a meshfree peridynamic code*, Fluid and Solid Mechanics (K. J. Bathe, ed.), vol. 1, Massachusetts Institute of Technology, Elsevier, June 2003.
23. S.A. Silling, *Reformulation of elasticity theory for discontinuities and long-range forces*, Journal of the Mechanics and Physics of Solids **48** (2000), no. 1, 175 – 209.
24. S.A. Silling and E. Askari, *A meshfree method based on the peridynamic model of solid mechanics*, **83** (2005), 1526–1535.
25. S.A. Silling, M. Epton, O. Weckner, J. Xu, and E. Askari, *Peridynamic states and constitutive modeling*, Journal of Elasticity **88** (2007), no. 2, 151–184 (English).
26. Schram; S.J. and Meyer H.W, *Simulating the formation and evolution of behind armor debris fields*, ARL-RP 109, U.S. Army Research Laboratory, 2005.
27. E. Strassburger, *Visualization of Impact Damage in Ceramics Using the Edge-On Impact Technique*, International Journal of Applied Ceramic Technology, vol. 1, 2004, pp. 1:235–242.
28. Tracy J. Vogler, Tom F. Thornhill, William D. Reinhart, Lalit C. Chhabildas, Dennis E. Grady, Leonard T. Wilson, Omar A. Hurricane, and Anne Sunwoo, *Fragmentation of materials in expanding tube experiments*, International Journal of Impact Engineering **29** (2003), no. 1–10, 735 – 746, Hypervelocity Impact.
29. Xiaotian ZHANG, Guanghui JIA, and Hai HUANG, *Fragment Identification and Statistics Method of Hypervelocity Impact SPH Simulation* , Chinese Journal of Aeronautics **24** (2011), no. 1, 18 – 24.